Volume 21 | Number 9 | 7 March 2019 | Pages 4675–5314

PCCP

Physical Chemistry Chemical Physics

rsc.li/pccp

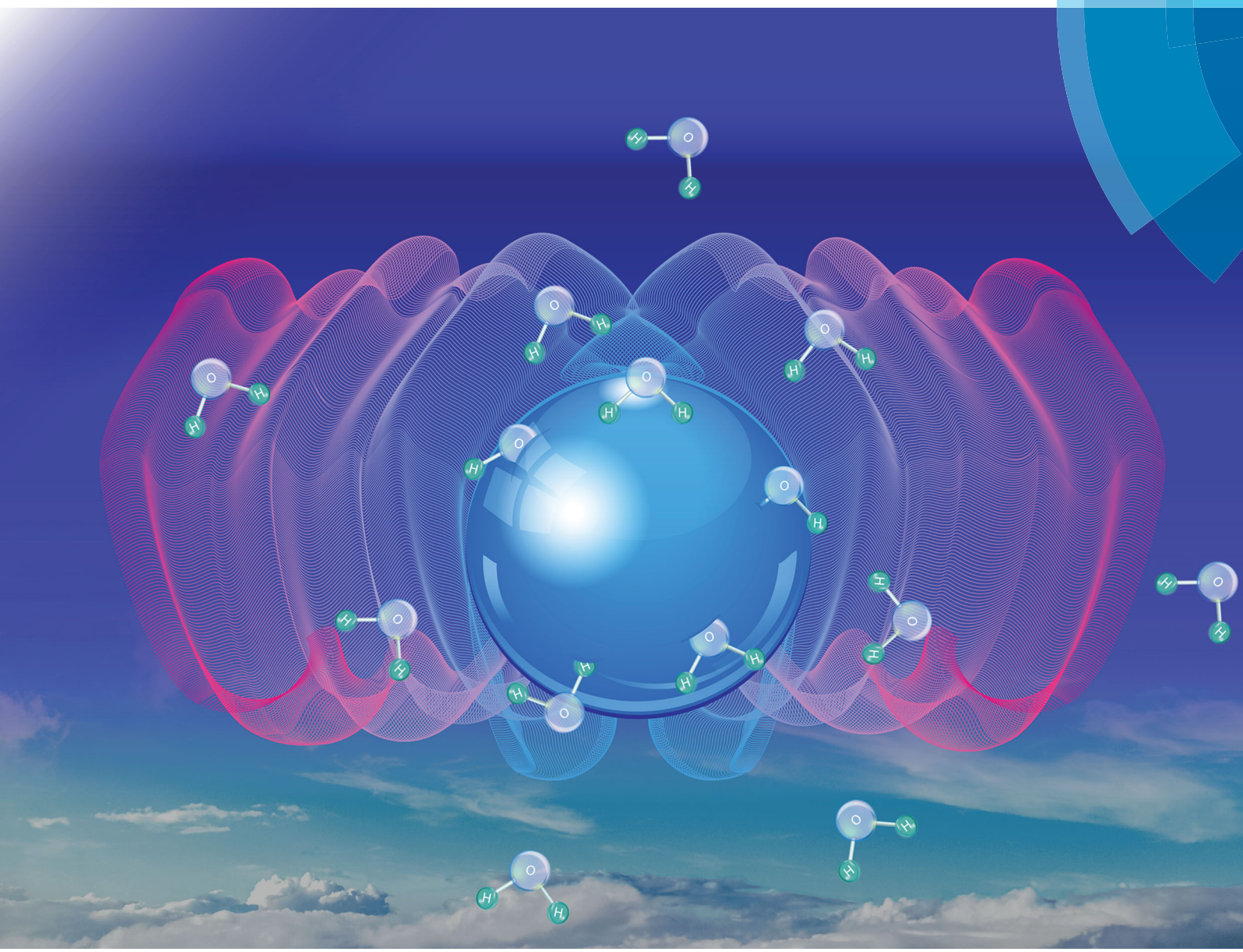

ISSN 1463-9076

ROYAL SOCIETY OF CHEMISTRY | Celebrating IYPT 2019

PAPER

Ruth Signorell *et al.*

Assessing relative humidity dependent photoacoustics to retrieve mass accommodation coefficients of single optically trapped aerosol particles

PCCP

PAPER

View Article Online
View Journal | View Issue

Cite this: *Phys. Chem. Chem. Phys.*, 2019, **21**, 4721

Assessing relative humidity dependent photoacoustics to retrieve mass accommodation coefficients of single optically trapped aerosol particles

Matus E. Diveky, † Sandra Roy, † Johannes W. Cremer, Grégory David and Ruth Signorell *

Received 10th November 2018,
Accepted 13th December 2018

DOI: 10.1039/c8cp06980h

rsc.li/pccp

Photoacoustic spectroscopy is widely used to measure the light absorption of aerosols. However, the impact of key factors such as the effect of relative humidity and mass exchange on photoacoustic measurements are still poorly understood. We assess such measurement biases and their physical origin by analysing the photoacoustic signal of single tetraethylene glycol (TEG) particles at varying relative humidities. Our results show a decrease in the photoacoustic signal at elevated relative humidities for small particles (0.8–1.5 μm), while for larger sizes (2.2–3.2 μm) the trend is reversed. We model the photoacoustic signal to interpret the observed behaviour in terms of mass and heat flux contribution. The single particle photoacoustic signal analysis presented in this paper additionally allows for the retrieval of the mass accommodation coefficient. Fitting our experimental data to the theoretical model reveals values of $\alpha_M \approx 0.02–0.005$ for water on TEG in the temperature range 295–309 K.

1 Introduction

Atmospheric aerosols play a major role in the Earth's radiative budget, yet questions regarding their exact contributions remain unanswered. The current estimates hint at an overall cooling effect of anthropogenic aerosols,[1] though there are significant uncertainties surrounding their direct, indirect and semi-direct effects.[2–4] The absorption and scattering of shortwave radiation by aerosols directly influences Earth's radiative forcing. The ice nucleation properties of aerosols and their propensity to act as cloud condensation nuclei can also modify the microphysical properties of clouds. New advances in experimental methods used for measuring the physical properties of aerosols are necessary to improve our current understanding of the role that aerosols play in atmospheric processes.[5]

Photoacoustic (PA) spectroscopy is a standout technique widely used for ensemble absorption measurements of atmospheric aerosols, both in laboratories and environmental campaigns.[6–13] The physical basis of photoacoustic spectroscopy is the conversion of modulated light energy into thermal energy. During a photoacoustic measurement, the modulated excitation laser is partially absorbed by the studied system leading to periodic heating and cooling of the system. This results in the formation of acoustic waves, due to the heat conduction from the studied system to the surrounding air (heat flux). The corresponding acoustic signal (sound) can be measured by a microphone or a piezoelectric tuning fork.[7,14] In addition to the heat transfer, the absorbed energy can be dissipated *via* evaporation of semi-volatile species, such as water (Fig. 1). This mass flux from the particle also contributes to the photoacoustic signal, however, its conversion efficiency

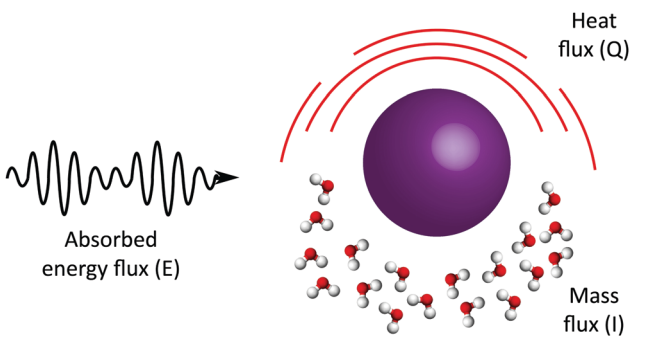

Fig. 1 Energy dissipation pathways. Absorbed energy from the incoming modulated laser can be dissipated *via* either heat flux *Q* or mass flux *I*. The heat flux represents the formation of acoustic waves due to periodic heating and cooling of the surrounding air. The mass flux corresponds to an evaporation of volatile species (*e.g.* water) from the aerosol droplet.

Laboratory of Physical Chemistry, Department of Chemistry and Applied Biosciences, ETH Zürich, Vladimir-Prelog-Weg 2, CH-8093 Zürich, Switzerland. E-mail: rsignorell@ethz.ch
† These authors contributed equally to this work.

to the photoacoustic signal is less when compared to that of the heat flux. This is due to the energy needed for the evaporation of the volatile species (latent heat). Theoretical models of mass flux contribution towards the photoacoustic signal show that this energy dissipation pathway becomes more pronounced at high relative humidities.[15–19]

Relative humidity (RH) plays a key role in defining the optical properties of atmospheric aerosols. The change induced in a particle's water content impacts its light absorption and scattering and hence its effect on the climate. The RH-dependence of aerosols' scattering has been extensively studied,[20–24] however the impact of RH on absorption is still a matter of debate. Several studies suggest that the absorption of different aerosols should increase with increasing RH.[25–28] For example, it has been shown that the absorption of light-absorbing carbon increases when the particles are mixed with non-absorbing species, such as water at visible wavelengths.[29] On the other hand, Willoughby *et al.* used laser-induced heating to determine the RH-dependence of the imaginary parts of the refractive index (RI) of single particles of NaCl and $(NH_4)_2SO_4$.[30] Their study suggests that for particles 1–2.2 μm in radius the absorption decreases with increasing RH, which they attribute to the presence of impurities.

Photoacoustic spectroscopy has also been used to measure the RH-dependence of aerosols' absorption. Arnott *et al.* used a flow-through photoacoustic spectrometer in field measurements to determine the absorption of black carbon at different levels of relative humidity.[31] They observed a systematic decrease in the PA signal when the RH increased beyond 70%. Another laboratory study of smoke particles performed by Lewis *et al.* measured a 20% decrease in the PA signal with increasing relative humidity.[32] Langridge *et al.* measured the PA signal of various absorbing aerosols as a function of RH and also observed a systematic decrease with increasing relative humidity.[33] This study further concluded that the PA spectroscopy is a valid technique for absorption measurements only when used in dry conditions. All of these authors proposed that the experimentally observed decrease in the PA signal is due to a more pronounced mass flux at elevated RHs. However, the photoacoustic studies on Saharan dust-dominated air mass carried out by Lack *et al.* showed an enhancement of the PA signal by a factor of 1.5 ± 0.3 with increased RH.[34] The current discussion in the literature regarding the impact of RH on the photoacoustic signal and the precise role of the mass flux is inconclusive.

In order to acquire a fundamental understanding of the PA signal generation, the first-ever single-particle photoacoustic spectrometer (SP-PAS) was reported in 2016 by Cremer *et al.*[35] This newly-developed instrument allows us to perform high-sensitivity *in situ* PA measurements on single, unsupported particles down to the submicron region. By studying single particles as opposed to ensembles, we avoid averaging effects and gain insights into the size-dependence of the PA measurements. For example, we investigated the size-dependence of the photoacoustic signal (PAS) and found that for particles larger than 1 μm in radius there is significant signal damping due to limited heat conductivity of the surrounding air.[36] Furthermore, performing single-particle PA spectroscopy allows for new types of measurements on aerosol particles, such as the determination of particle-size dependent reaction rates due to optical cavity effects.[35] In addition, performing cavity ring-down spectroscopy on single aerosol particles proved to be a powerful tool to measure optical properties of aerosols and their dynamics.[37,38]

The single-particle nature of our measurements is achieved by the introduction of an optical trap to the set-up. We use counter propagating tweezers (CPT) which enables the trapping of micron and submicron particles with tight particle confinement, allows for long working distance and has a relatively straightforward alignment procedure.[39–42] Many other optical traps are available,[43] however CPT trap is the most suited for our purposes due to aforementioned advantages. One of the aims of the work presented in this paper is to study the photoacoustic response of optically-trapped particles at different relative humidities. In addition, the analysis of the mass flux component from such studies provides an experimental window into the kinetics of water condensation and evaporation from an aerosol particle.

The mass accommodation coefficient (α_M) is a kinetic parameter describing the probability of gas-phase molecule accommodation onto an aerosol surface upon collision. Knowing the exact values of mass accommodation coefficients for various systems is important for accurate climate modelling and predictions. Numerous studies have measured the mass accommodation coefficient of water vapour on the surface of liquid water, however, significant uncertainty in the exact value still remains.[44–54] Many such studies are summarised in the review by Kolb *et al.*[55] The determination of α_M of various organic compounds, such as glycols, has also been the subject of several studies.[46,56–58] Uptake coefficients of trace gases onto atmospheric aerosols, which are equal to the mass accommodation coefficients for Knudsen numbers $\gg 1$,[17] are also discussed in reviews by Kolb *et al.*[55] and Abatt *et al.*[59]

In this work we also assess the performance of single-particle photoacoustic spectroscopy in retrieving mass accommodation coefficients of water vapour on tetraethylene glycol particles. In principle, the high sensitivity of photoacoustics allows for low laser powers to be used and hence restricts the temperature oscillation to just a few Kelvins. In addition, a high modulation frequency keeps the total mass flux small and hence SP-PAS allows us to work near equilibrium conditions. By incorporating a stable CPT trap, we can vary the radius of the particles from the micron to the submicron regime. A comparison with ensemble studies[47] enables one to gain insights into number- and size-averaging effects and their impacts on α_M retrieval.

To the best of our knowledge, this is the first study that measures the mass accommodation coefficient of water vapour on single organic aerosols. Retrieval of mass accommodation coefficients for such heterogeneous systems is of huge importance for atmospheric sciences as the kinetics of water condensation on particles plays a key role in defining activated aerosol concentration in the atmosphere.[55,60–63] This work is also the first

assessment of the RH dependence of single particle photoacoustics. In this work we present the photoacoustic spectra obtained at different RHs together with the results from theoretical modelling. Through the comparison of the experimental and theoretical data we retrieve the value of the mass accommodation coefficient for our system.

2 Experimental

2.1 Optical trapping

Aerosol particles of tetraethylene glycol (TEG, Acros Organics) were introduced into the optical trap using a customised nebuliser. TEG was chosen as a model organic substance because of its low vapour pressure required for optical trapping, its hygroscopic nature allowing RH-dependent measurements and its well documented physical properties needed for modelling. Single droplets of TEG were trapped in the centre of an acoustic resonator through the use of cross polarised counter-propagating tweezers (CPT). In this configuration (Fig. 2), a 532 nm trapping laser (Laser Quantum, Opus) is linearly polarised at 45° using a half wave plate (Thorlabs, WPH10M-532) and expanded to 7.4 mm in diameter using a telescope. The beam is then divided in two gaussian beams with identical intensity (~250 mW) using a polarisation beamsplitter (Thorlabs, PBS201). The trapping beams are directed to both sides of the PA cell and tightly focused with 75 mm aspherical lenses (Thorlabs, ASL10142).

Measurements of single particles with variable sizes in a gas flow environment are prone to positioning instability.[64] This is observed as a displacement of the particle along the direction of beam propagation as the size of the particle changes. For single-particle photoacoustic measurements, it is essential that the particle remains well-confined, otherwise the displacement of the particle within the excitation beam is apparent in the PA signal.[65] To counteract this movement, a feedback system was put in place. An electro-optic modulator (EOM, ConOptics) was placed before the polarisation beamsplitter to control the light polarisation and thus control the relative intensity of both trapping beams. A quadrant photodiode (Hamamatsu, S5980) placed after the objective (Fig. 2 left) was used to monitor the position of the particle. The information from the quadrant photodiode was then relayed every 0.25 ms to a PID controller that corrects any movement by adjusting the voltage applied to the EOM. This position-confinement technique has shown to greatly enhance the stability of the particle.

All experiments were performed in a nitrogen environment with a constant total flow of 20 sccm. To avoid disturbing the particle, an indirect flow was chosen. As seen in the middle of Fig. 2, the aerosol and flow inlet/outlet are both situated in the same buffer volume only allowing diffusion into the acoustic resonator. The relative humidity was adjusted by mixing dry and water saturated nitrogen flows. The temperature and the relative humidity of the system were monitored with a sensor placed in the other buffer volume, ~2 cm away from the particle with 0.3 K and 2% accuracy. To ensure that a proper equilibrium within the cell was achieved, only measurements in which the relative humidity stayed constant within ±0.4% were analysed.

2.2 Photoacoustics

Single particle photoacoustic spectroscopy was performed using a specifically designed resonant photoacoustic cell (Fig. 2 right).[8,35,66] This cell was designed to allow optical trapping, photoacoustic measurements and elastically scattered light collection. The two buffer volumes inside the cell serve as acoustic noise reducers. The photoacoustic signal is induced by a focused IR laser (9.47 μm diode laser from AdTech Optics) and measured by an electret microphone (Knowles Electronics, EK-23133-C36).

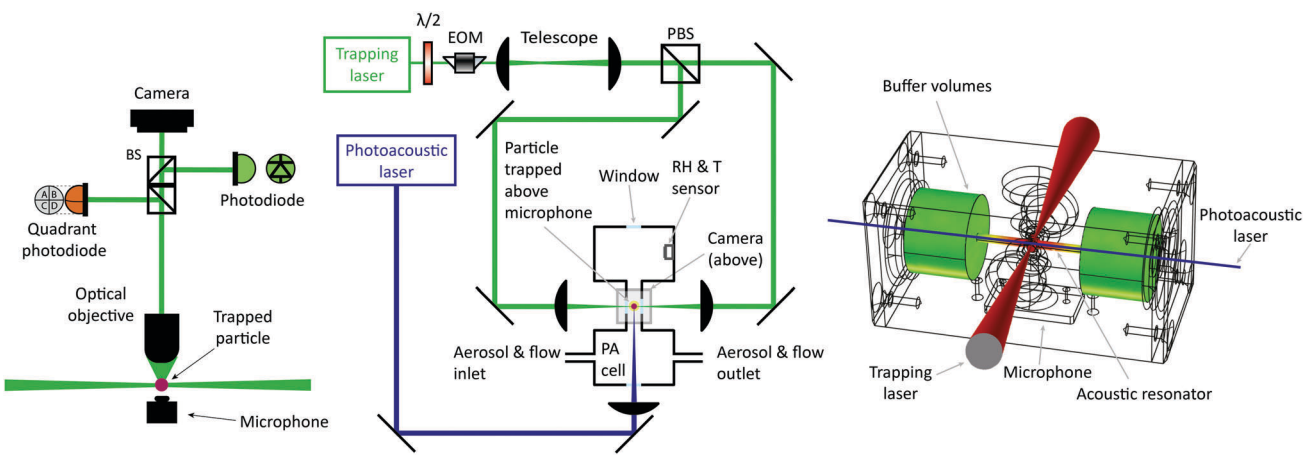

Fig. 2 Experimental set-up used for single-particle photoacoustic spectroscopy. Left: Side view of the optical set-up collecting scattered light from the particle and projecting it onto a quadrant photodiode, a camera and a photodiode. Centre: Top view of the optical table comprising of a trapping laser (green), photoacoustic laser (blue), the PA cell and a trapped particle (red). The trapping laser is expanded using a telescope and the relative intensities of the two trapping beams are controlled by the electro-optic modulator (EOM). Right: The photoacoustic cell used in these experiments showing the trapping laser (red), the photoacoustic laser (blue), buffer volumes and a microphone. The colour scheme inside the cell represents the acoustic intensity originating from the particle. Figure adapted from ref. 35 (This work is licensed under a Creative Commons Attribution 4.0 International License; http://creativecommons.org/licenses/by/4.0/).

The power of the IR laser at the particle is 7.1 ± 0.2 mW and its diameter is 153 ± 6 μm. The microphone is located directly underneath the trapped particle (see Fig. 2 right). The laser is modulated at 4 kHz to match the resonant frequency of the 4 cm long acoustic resonator, in which the particle is trapped. The microphone signal is demodulated using a lock-in amplifier (Zurich Instruments, 500 kHz MFLI).

The photoacoustic IR laser resonant with an absorption at 1056 cm^{-1} of TEG was shone on the trapped particle producing a PA signal and causing the particle to shrink in size. The PA signal was measured with a time constant of 300 ms for approximately 10 minutes. Because of low vapour pressure of TEG, the particles do not shrink noticeably during one PA data collection (300 ms). The many data points taken over time (10 min) correspond to PA measurements for a range of different particle sizes. At the end of the measurement, the particle was ejected from the trap and the PA background was measured. During the data analysis, this background was subtracted from the raw PA signal. Multiple single particle measurements were collected at a given RH to provide statistically relevant results.

2.3 Modelling

A theoretical model based on thermal conduction (Fourier's law) and molecular diffusion (Fick's law) in the surrounding gas with transition flow corrections was developed to simulate the photoacoustic signal of spherical symmetric droplets as a function of particle size for different relative humidities.[19,36]

As aforementioned, absorbed energy can be dissipated in two ways, heat flux (Q) and mass flux (I). The heat flux can be expressed as a function of the particle temperature (T_a)

$$Q \approx 4\pi r K \beta_T (T_a - T_\infty) \quad (1)$$

where r is the particle radius, K is the heat conductivity of the surrounding gas, β_T is the thermal transition flow correction factor and T_∞ is the ambient temperature. The mass flux can be described with the linearised mass diffusion equation combined with the Claussius–Clayperon equation

$$I \approx 4\pi r D \beta_M \frac{p_v M_v}{RT_\infty^2}\left(\frac{LM_v}{RT_\infty} - 1\right)(T_a - T_\infty) \quad (2)$$

where D is the diffusion coefficient of water in air, β_M is the mass transition flow correction factor, p_v is the partial pressure of water vapour, M_v is the molar mass of the evaporating species (water), R is the universal gas constant and L is the heat of vaporisation of water. The transition flow correction factors are calculated through[16,50]

$$\beta_i = \frac{1 + Kn_i}{1 + \left(\frac{4}{3\alpha_i} + 0.377\right)Kn_i + \frac{4}{3\alpha_i}Kn_i^2} \quad \text{where } i = T, M \quad (3)$$

where Kn_T and Kn_M are the Knudsen numbers and α_T and α_M are the thermal and mass accommodation coefficients, respectively.

$$Kn_T = \lambda_g / r$$
$$Kn_M = \lambda_v / r \quad (4)$$

where λ_g and λ_v are the mean free path of the gas molecules and vapour molecules in air, respectively. The amplitude of the photoacoustic signal is correlated to the variation in Q and I through

$$S \propto \Delta V = \frac{R}{p}\left(\frac{\Delta Q}{M_g c_{p,g}} + \frac{\Delta I T_\infty}{M_v}\right) \quad (5)$$

where M_g is the molecular mass of the surrounding gas and $c_{p,g}$ is the heat capacity of the gas.

This variation in Q and I are related to the temperature oscillation of the particle (ΔT_a)

$$\Delta T_a = \frac{I_0 C_{abs}}{4\pi r K |1 + f_M - i\omega\tau|} \quad (6)$$

$$\tau = \frac{r^2 \rho_a c_{p,a}}{3K} \quad (7)$$

$$f_M = \frac{\beta_M}{\beta_T}\frac{L D p_v M_v}{K R T_\infty^2}\left(\frac{LM_v}{RT_\infty} - 1\right) \quad (8)$$

where τ is the time constant for the thermal inertia of the particle, f_M is the ratio of energy fluxes due to heat and mass transport, I_0 is the PA laser amplitude, C_{abs} is the absorption cross section of the particle which is radius-dependent, ρ_a is the particle density, $c_{p,a}$ is the specific heat capacity of the particle and ω is the angular modulation frequency. The absorption cross section of the particle was determined using Mie theory and the complex refractive index of the particle.

Despite the particle's change in temperature at 4 kHz, all physical constants were considered at the particle average temperature ($\overline{T_a}$). When modelling the photoacoustic signal of aerosol particles, it is also important to consider their hygroscopic nature. Since TEG is hygroscopic, the particle composition depends on the relative humidity. As the relative humidity is changed, the composition is altered, impacting the particle's physical properties such as the complex refractive index, density, heat capacity, absorption cross section and ultimately the particle average temperature. In addition, the average temperature of the particle changes with its size

$$\overline{T_a} = \frac{I_0 C_{abs}}{4\pi r K (1 + f_M)} + T_\infty \quad (9)$$

Changing particle average temperatures can in turn alter the physical properties of the aerosol. To account for these code-dependent effects, we followed an iterative modelling approach recalculating the physical properties from $\overline{T_a}$ until self-consistency was reached. Fig. 3 shows the resulting particle temperature and composition for different sizes and relative humidities. The temperature seems to have close to a linear dependence on the particle radius, independently of the relative humidity. On the other hand, the change in the particle composition is more pronounced with increasing relative humidity. For 90% relative humidity, the water concentration increases by ~30 percent by mass from large to small particles. However, for relative humidities lower than 60% the concentration changes are within a few percent by mass.

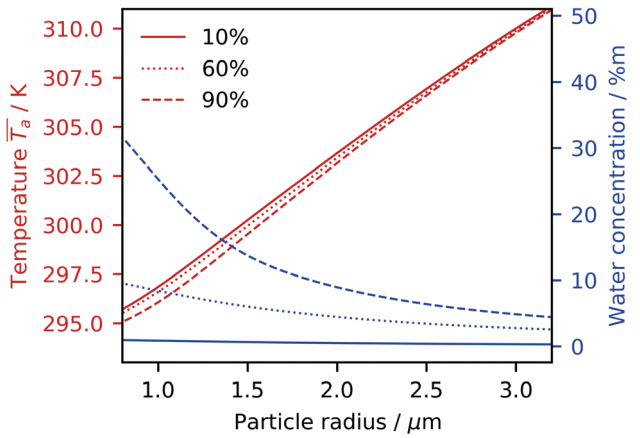

Fig. 3 Modelling of the size dependent temperature and water concentration of TEG aerosols. Simulations at different relative humidities are shown – solid line (10%), dotted line (60%) and a dashed line (90%).

Table 1 Physical constants used in the modelling

Constant	Value	Ref.
T_∞	293.7 K	
M_g	28.00 g mol^{-1}	
M_v	18.02 g mol^{-1}	
R	8.314 J mol^{-1} K^{-1}	
K	0.02597 W m^{-1} K^{-1}	67
D	2.49 × 10^{-5} m^2 s^{-1}	19
L	2450 kJ kg^{-1}	19
p	1.014 × 10^5 Pa	
$c_{p,g}$	1004 J kg^{-1} K^{-1}	67

Table 2 Temperature and composition dependent physical constants used in the modelling

Constant	Value$_W$	Value$_{TEG}$	Ref.
ρ	0.998 g cm^{-3}	1.124 g cm^{-3}	68
$n + ik_{532nm}$	1.3337 + 1.4992 × 10^{-9}i	1.4623 + 2.48 × 10^{-8}i	68
$n + ik_{9.47\mu m}$	1.2442 + 0.044035i	1.412 + 0.5411i	
p_v	2.3393 kPa		67
$c_{p,g}$	4181 J kg^{-1} K^{-1}	2140 J kg^{-1} K^{-1}	67 and 69

Table 1 lists important physical constants at room temperature and ambient pressure used in the model. Table 2 presents the temperature and composition dependent variables, values are shown for pure substances at room temperature.

The refractive index of the water–TEG mixture was calculated using the Lorentz–Lorenz effective medium approximation.[70] The temperature dependence of the composition, refractive index and density was parametrised according to ref. 68. The imaginary part of TEG refractive index was evaluated from ATR-IR measurements. The complex refractive index of TEG at 532 nm as well as the real part of the refractive index at 9.47 μm was estimated from values of ethylene glycol[71] combined with the ratio of ethylene glycol to TEG at 589 nm.

2.4 Size fitting

Particle sizes were determined from the elastic scattering of the trapping laser. The optical objective above the PA cell collects scattered light over an angle of 49.6° and projects it onto a quadrant photodiode, a camera and a photodiode (Fig. 2 left). The time evolution of the total light intensity recorded by the photodiode (sampling frequency of 100 Hz) is fitted to Mie theory. A parametrised double exponential function is used to represent the radius change in time. For each set of parameters considered, a theoretical phase function is interpolated from the pre-calculated Mie pattern and compared with the experimental one. The agreement between the fit and the experiment is measured by the sum of squares (SSQ) to find the optimal parameters.

For each relative humidity, the composition of the particle (TEG/H_2O ratio) is calculated in order to use the correct optical parameters for the size fitting. Furthermore, as the particle shrinks, its elevated temperature ($\overline{T_a}$) decreases which results in the change of its refractive index at 532 nm (Fig. 3). Hence both the RH-dependence and the time-dependence of the refractive index must be considered in the size retrieval.

3 Results and discussion

3.1 Effect of relative humidity on photoacoustics

Photoacoustic spectra of single optically trapped aerosol particles were recorded at different relative humidities. The size evolution of over 390 particles at 29 different relative humidities was calculated and the corresponding photoacoustic data was analysed. Fig. 4 (top) shows averages of multiple single-particle PA measurements against particle radius for 6 different RH. The results are divided into two radius ranges – 0.8 to 1.5 μm (left) and 1.5 to 3.2 μm (right) – as we observe two different behaviours for the two size ranges. These two size regimes will be discussed separately. Furthermore, the results from the theoretical model (described in Section 2.3) are also shown in Fig. 4. The simulation is shown for two different values of α_M, which will be discussed in Section 3.2.

In general, we observe a decrease in the photoacoustic signal with decreasing radius of a particle. This is due to smaller absorption cross sections of smaller particles. In addition, we notice that the PA signal varies with different relative humidities. This can be explained by a change in the composition of the particle. Both the absorption cross section of particles and the relative distribution of the two energy dissipation pathways (heat flux Q and the mass flux I shown in Fig. 1) are affected by the composition change of a particle.

Small radii. For particles in the size range of 0.8–1.5 μm (Fig. 4 left) we observe a decrease in the PA signal with increasing RH. As the water content of the particles increases with the increasing RH, the absorption cross section of the droplets decreases. Smaller absorption of the photoacoustic IR laser at elevated RH results in less photoacoustic signal. Furthermore, higher water content of the TEG droplets leads to an elevated mass flux to the detriment of the heat flux. Under our experimental conditions, we are much more sensitive to the heat flux than to the mass flux due to a high latent heat of water. Hence any redistribution of energy from the heat flux

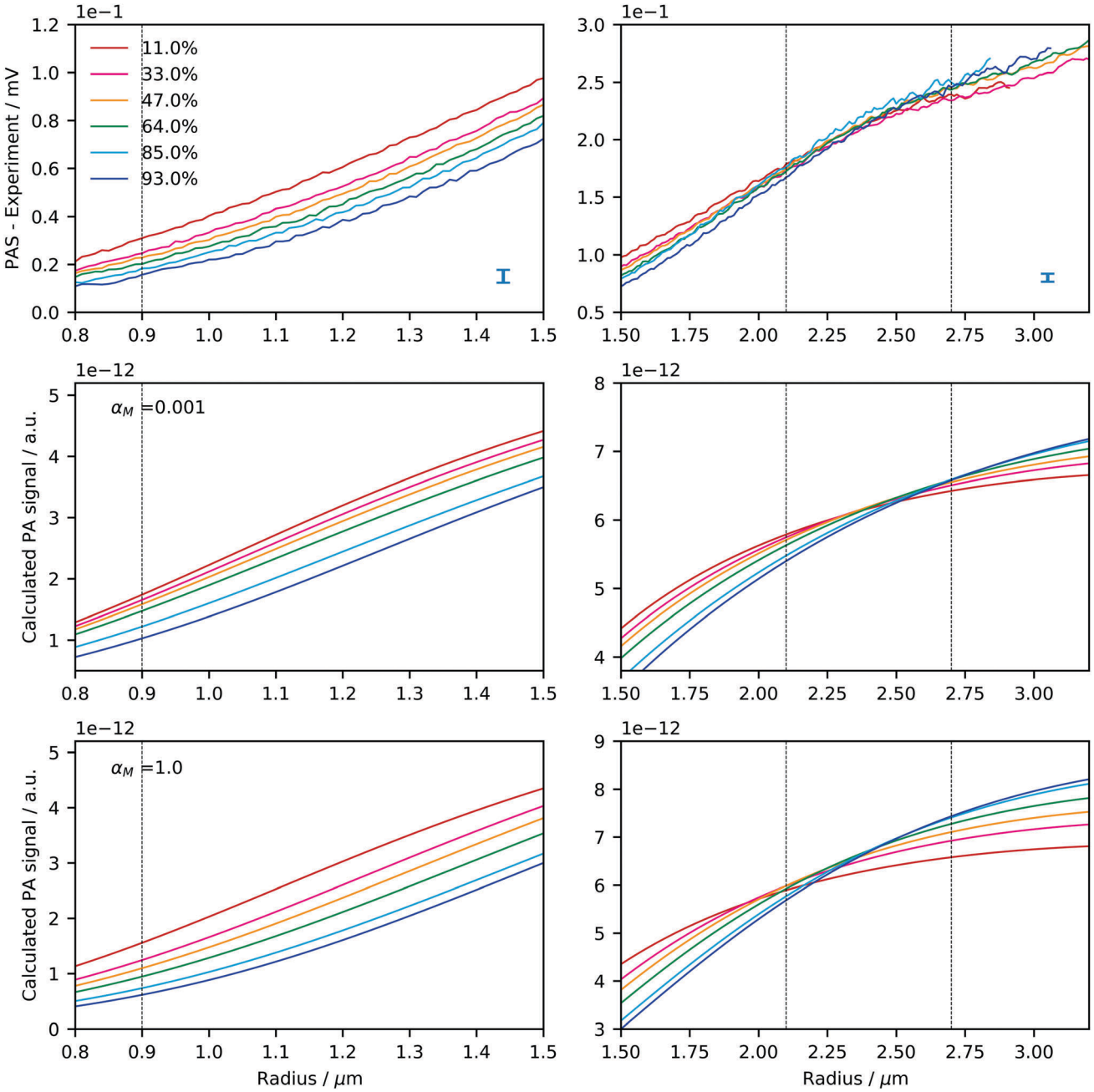

Fig. 4 Experimental (top) and calculated (middle & bottom) size dependent photoacoustic signals for different relative humidities. The measured and simulated photoacoustic signals at 11, 33, 47, 64, 85 and 93% RH are shown. The simulation was run for two different values of mass accommodation coefficients (α_M = 0.001 and α_M = 1.0). Average error bars are shown at the bottom right corner for both radii range. The dashed vertical lines represent radii which were selected for further analysis shown in Fig. 6.

into the mass flux results in smaller photoacoustic signal measured. To quantify the observed decrease, a 1 μm particle experiences a difference in the photoacoustic signal of approximately 59% between dry (11% RH) and wet (93% RH) environments while the modelled absorption cross section decreases by 33%. This significant discrepancy between the photoacoustic signal and the absorption change needs to be taken into account when measuring absorption of atmospheric aerosols.

For all values of α_M, the theoretical results show similar qualitative trends as the experiment; predicting a significant decrease in the photoacoustic signal with increasing RH. To further understand this behaviour, the modelled photoacoustic signal was separated into its two components – the heat flux (Q) and the mass flux (I). These are plotted against the particle radius in Fig. 5. For small particles, we see a large decrease in the photoacoustic signal originating from the heat flux (solid lines) with increasing RH. When considering the photoacoustic

signal from the mass flux (dash lines), we only observe a small increase at high RH. When considering both of the components combined, we see that with increasing relative humidity the overall photoacoustic signal decreases as the increase in the mass flux component does not compensate for the decrease in the heat flux contribution.

Large radii. For particles in the size range of 1.5–3.25 μm (Fig. 4 right), we observe a different behaviour compared to that of small particles. The photoacoustic signal dependence upon the RH changes throughout this size regime, with a crossing of the signals in the range of 2.1–2.6 μm. Before this crossing, we observe decreasing photoacoustic signal with increasing RH. However, for the particles larger than ~2.6 μm we notice a reversal in the PA–RH trends with an increase in the photoacoustic signal at elevated RH. The theoretical results from the simulation show the same behaviour of increasing photoacoustic signal with increasing RH for large particles. The α_M-dependent crossings between the individual curves is also clearly visible in the simulation.

To understand the observed reversal in the PA–RH trend for large particle radii, we can again consider the relative contributions of the heat flux and the mass flux (Fig. 5). Looking at the heat flux contribution to the photoacoustic signal (solid lines), we see that this component plateaus at large radii for all relative humidities. This dampening effect happens because of the hindered heat dissipation from the particle, which starts to be significant for particles larger than 1 μm in radius. This phenomenon occurs due to a limited heat conductivity of the surrounding air and is discussed in detail in ref. 36. Furthermore, we see that the decrease in the heat flux contribution with increasing RH gets smaller for larger radii. On the contrary, the photoacoustic signal from the mass flux component increases significantly with increasing RH for large particles. When both of these contributions are considered, we can understand why for large particles the photoacoustic signal increases with increasing relative humidity. This is despite the decreasing absorption cross section of the particle. As an example, for a particle radius of 2.7 μm, the photoacoustic signal increases by 7% between dry and wet environments, while the C_{abs} decreases by 2%.

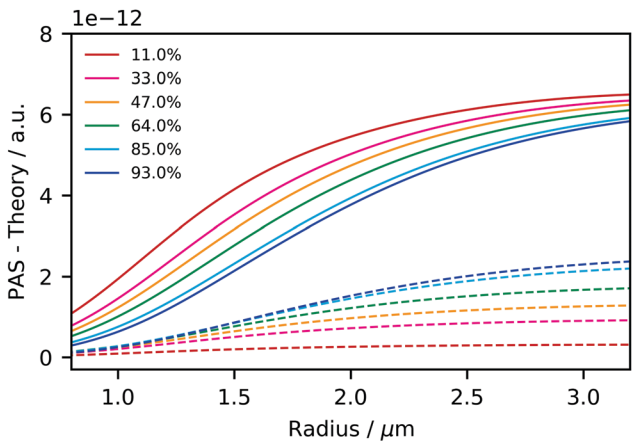

Fig. 5 Calculated size dependent photoacoustic component signals for different relative humidities. The dashed line corresponds to mass flux (*I*) contribution and the solid line corresponds to the heat flux (*Q*) contribution to the photoacoustic signal. This data was calculated for α_M = 1.0.

Discussion. This is an unexpected finding which to the best of our knowledge has never been directly stated in the literature. The dependence of the PA–RH trend upon particle sizes is a newly discovered phenomena which has to be taken into account to accurately interpret the absorption measurements of atmospheric aerosols measured by photoacoustic spectroscopy. In principle, these results could explain the discrepancies in the literature over the exact effect of relative humidity on the photoacoustic signal. The photoacoustic studies of hygroscopic aerosols at varying RH done by Langridge *et al.*[33] and Lewis *et al.*[32] were performed on particle ensembles smaller than 1 μm. These laboratory studies showed a decrease in PAS with increasing RH, which is consistent with our size dependent findings. On the other hand, photoacoustic field studies performed with a 10 μm cut point showed both an increase[34] and a decrease[31] of the PA signal at elevated RH. As these two studies were sampling a broad size-range of aerosols, it is possible that both effects – the PA signal enhancement and reduction at elevated RH – were taking place. The reason behind the different findings of these two studies might be different size distributions of the studied systems. However, it is also important to keep in mind that the reversal of the PA–RH trend might appear at different sizes for different systems. The position of the crossing depends both on the physical properties of the studied aerosols (such as hygroscopicity and complex refractive index) and on the design of the photoacoustic spectrometer (mainly power and modulation frequency of the excitation laser). These properties alter the light absorption of particles which in turn impact the temperature oscillation (ΔT_a) and the average temperature ($\overline{T_a}$) of the particle (see eqn (6) and (9) respectively.) These quantities influence the RH-dependence of photoacoustics through the heat and mass flux contributions.

The work presented in this paper reveals the size dependent trends in the PA–RH behaviour and shines new light onto the current discussion about the exact impacts of RH on the PA signal. However, to explain the findings reported by other authors mentioned above on a fundamental level, one would have to investigate the specific systems (the aerosol type and the type of the spectrometer used) on a single-particle level.

3.2 Accommodation coefficient

The mass accommodation coefficient influences the kinetics of water evaporation/condensation (mass flux) on the particle's surface. The photoacoustic signal is sensitive to the mass accommodation coefficient through its mass flux contribution, as can be seen in the eqn (2) and (3). Fig. 4 (middle and bottom) shows the simulated PA signal as a function of particle radius for α_M values of 0.001 and 1.0. The simulations shown were performed for six different relative humidities. The theoretical results reveal that the value of the mass accommodation coefficient influences the shape of the

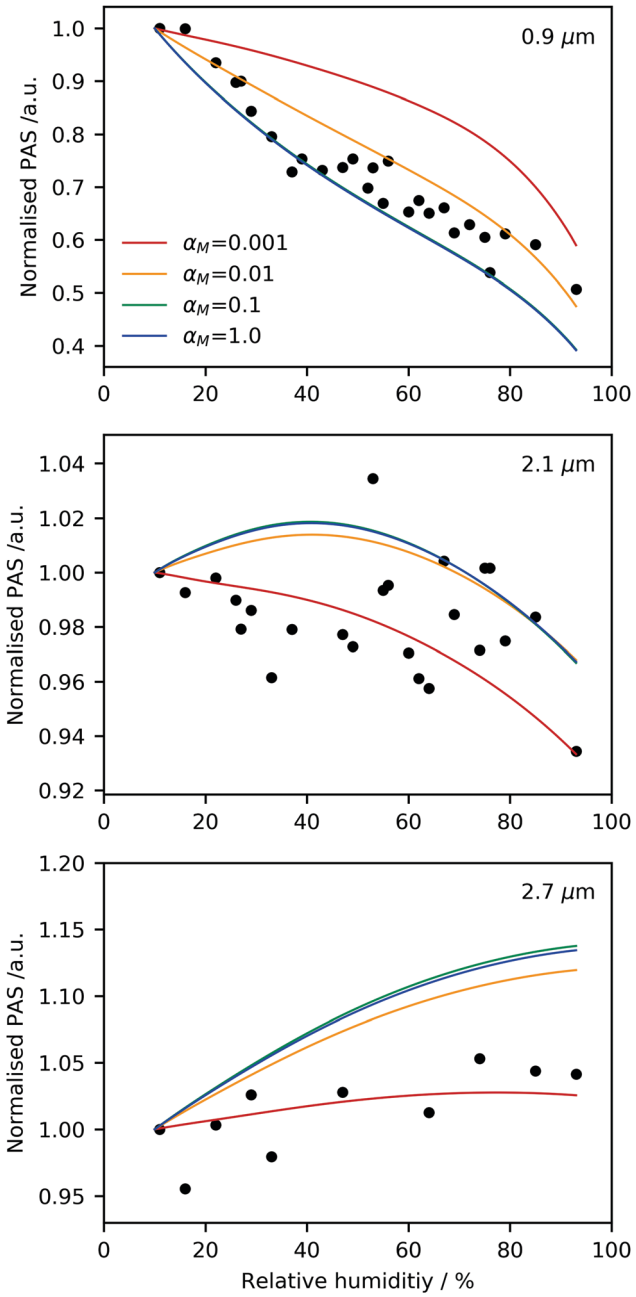

Fig. 6 Experimental (dots) and calculated (solid lines) relative humidity dependent photoacoustic signals for different sizes. The modelling was performed at four different mass accommodation coefficient values (0.001, 0.01, 0.1 and 1.0) Note that α_M = 0.1 and α_M = 1.0 curves overlap.

individual curves and the particle size range within which the crossing of the PA signals appears.

Fig. 6 shows both the experimental (dots) and theoretical photoacoustic signal (solid lines) as a function of relative humidity for selected particle radii. The model is presented at four different α_M values. The experimental values are averages of multiple measurements at a given size plotted for up to 29 different relative humidities. All the photoacoustic data is represented normalised to the dry particles where the effect of the mass flux is insignificant. As previously observed, we can see the size dependent PAS–RH trend. For 0.9 μm radius particles (Fig. 6 top), we see a decreasing photoacoustic signal with increasing relative humidity both in the experimental data and the theoretical simulations for all α_M values. However, for particles 2.7 μm in radius (Fig. 6 bottom), we see a reversal in this trend. Furthermore, the photoacoustic signals at α_M = 0.1 and α_M = 1.0 seem to overlap through all relative humidities for small particle sizes (0.9 and 2.1 μm in Fig. 6), while for larger particles (2.7 μm in Fig. 6) these signals start to differ at higher relative humidities. This is likely due to a more pronounced mass flux at larger particle sizes, as can be seen in Fig. 5.

To retrieve the mass accommodation coefficient, a fit of the experimental data to the theoretical model was performed by minimising the weighted sum of the square deviations (χ^2) as a function of α_M for each value of the particle radius. The individual weights of the averaged data points are based on the experimental variations. Fig. 7 shows the resulting accommodation coefficient along with the upper and lower confidence intervals found through the fitting. The calculated confidence intervals correspond to a variation of χ^2 by 10^{-4}. The size range 1.7–2.3 μm was excluded from the fit, because the experimental noise precludes the determination of the weak RH dependence in this size range (see Fig. 4 top right). Fig. 7 shows a general decrease of the α value with increasing size. For small particles, we find an accommodation coefficient value around $\sim$0.02, while for larger particles the values decrease to less than 0.005. This could be related to the particle temperature or composition that changes as a function of the particle size. Fig. 7 also shows the average temperature of the particle for the specific sizes (upper x-axis). The data shows an inverse correlation between the accommodation coefficient and the particle temperature. This same trend has been observed in the literature for the mass accommodation coefficient of water and other components.[44,51,72] We can infer from our data that the mass accommodation coefficient of water on aqueous TEG

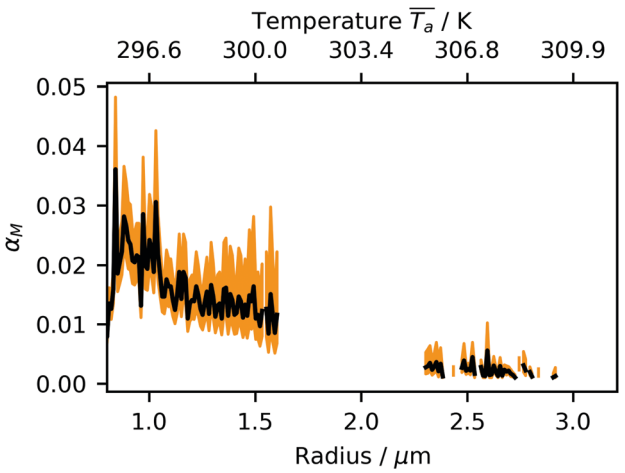

Fig. 7 Mass accommodation coefficient found from the fit at each radius. The upper x-axis shows the particle temperature for the different sizes. The black line represents the mass accommodation coefficient value and the orange band represents the confidence interval. Values between 1.7–2.3 μm were omitted due to large uncertainties.

particles lies between ~0.02 and 0.005 at temperatures between 295–309 K.

The mass accommodation of water on aerosol particles has not received much attention in the literature as of now due to the complexity of its determination. However, these values are of great importance for analysing the activation of atmospheric aerosols. Rudolf *et al.* has shown that for mass accommodation coefficients of water less than 0.1, the exact value of α_M can have a big impact on the number concentration of cloud droplets.[60] The technique described in our work could be a way towards assessing the aerosol activation effects by accurately determining α_M of water on different systems.

4 Conclusions

We have collected the photoacoustic signal of single TEG particles at varying RH (11–93%) for varying sizes (0.8–3.2 μm). Our results show that the influence of the relative humidity on the photoacoustic signal is particle size dependent. The change in the contribution of the heat flux and the mass flux induces a reversal in the PAS–RH correlation. For particles smaller than ~2.1 μm in radius, the photoacoustic signal decreases with increasing relative humidity, while for particles larger than ~2.6 μm, the trend is reversed. These results could possibly be applied to field measurements to correct for the effect of relative humidity on the photoacoustics signal. However, as the PAS–RH dependence is system specific, new single particle measurements should be carried out for different systems.

From fitting of our measurements to modelled data, we were able to extract the value of the mass accommodation coefficient of water on TEG particles. The value was found to be dependent on the particle's temperature and varied between 0.005–0.02 in the temperature range 295–309 K. This is, to the best of our knowledge, the first determination of mass accommodation coefficient through photoacoustic measurements on single aerosol particles. Photoacoustic experiments on single aerosol particles at varying RH could become a great tool in assessing the mass accommodation coefficient of water on mixed systems. This would allow for better insight into the aerosol activation events in the atmosphere.

We intend to further this technique by using a tuning fork as a photoacoustic sensor instead of a microphone.[35] As a result of the tuning fork's superior sensitivity, this would allow us to make measurement with lower irradiation intensity leading to smaller temperature deviation, and hence smaller variation in the physical properties of the particle. Furthermore, using a higher modulation frequency would minimise both the heat and mass flux and hence allows us to study the system closer to equilibrium.

Conflicts of interest

There are no conflicts to declare.

Acknowledgements

This work was supported by the Swiss National Science Foundation (grant no. 200020_177479) and ETH Research Grant ETH-42 18-1. We would like to thank Markus Steger and David Stapfer from the Laboratory of Physical Chemistry ETHZ for technical support. We would like to acknowledge discussions with our project partners, Prof. Christoph Haisch and Emilio Ambra. We are also thankful to Alexandra Bernasconi for performing initial test measurements and to Dr David Luckhaus for interesting discussions about the data analysis.

References

1 A. M. Fiore, V. Naik, D. V. Spracklen, A. Steiner, N. Unger, M. Prather, D. Bergmann, P. J. Cameron-Smith, I. Cionni, W. J. Collins, S. Dalsøren, V. Eyring, G. A. Folberth, P. Ginoux, L. W. Horowitz, B. Josse, J.-F. Lamarque, I. A. MacKenzie, T. Nagashima, F. M. O'Connor, M. Righi, S. T. Rumbold, D. T. Shindell, R. B. Skeie, K. Sudo, S. Szopa, T. Takemura and G. Zeng, *Chem. Soc. Rev.*, 2012, **41**, 6663–6683.

2 J. Haywood and O. Boucher, *Rev. Geophys.*, 2000, **38**, 513–543.

3 U. Lohmann and J. Feichter, *Atmos. Chem. Phys.*, 2005, **5**, 715–737.

4 D. Koch and A. D. Del Genio, *Atmos. Chem. Phys.*, 2010, **10**, 7685–7696.

5 T. C. Bond, S. J. Doherty, D. W. Fahey, P. M. Forster, T. Berntsen, B. J. Deangelo, M. G. Flanner, S. Ghan, B. Kärcher, D. Koch, S. Kinne, Y. Kondo, P. K. Quinn, M. C. Sarofim, M. G. Schultz, M. Schulz, C. Venkataraman, H. Zhang, S. Zhang, N. Bellouin, S. K. Guttikunda, P. K. Hopke, M. Z. Jacobson, J. W. Kaiser, Z. Klimont, U. Lohmann, J. P. Schwarz, D. Shindell, T. Storelvmo, S. G. Warren and C. S. Zender, *J. Geophys. Res.: Atmos.*, 2013, **118**, 5380–5552.

6 H. Moosmüller, R. K. Chakrabarty and W. P. Arnott, *J. Quant. Spectrosc. Radiat. Transfer*, 2009, **110**, 844–878.

7 C. Haisch, *Meas. Sci. Technol.*, 2012, **23**, 012001.

8 C. Haisch, P. Menzenbach, H. Bladt and R. Niessner, *Anal. Chem.*, 2012, **84**, 8941–8945.

9 D. A. Lack, M. S. Richardson, D. Law, J. M. Langridge, C. D. Cappa, R. J. McLaughlin and D. M. Murphy, *Aerosol Sci. Technol.*, 2012, **46**, 555–568.

10 M. Gyawali, W. P. Arnott, R. A. Zaveri, C. Song, H. Moosmüller, L. Liu, M. I. Mishchenko, L.-W. A. Chen, M. C. Green, J. G. Watson and J. C. Chow, *Atmos. Chem. Phys.*, 2012, **12**, 2587–2601.

11 B. Mason, N. L. Wagner, G. Adler, E. Andrews, C. A. Brock, T. D. Gordon, D. A. Lack, A. E. Perring, M. S. Richardson, J. P. Schwarz, M. A. Shook, K. L. Thornhill, L. D. Ziemba and D. M. Murphy, *Aerosol Sci. Technol.*, 2018, **52**, 1012–1027.

12 C. Linke, I. Ibrahim, N. Schleicher, R. Hitzenberger, M. O. Andreae, T. Leisner and M. Schnaiter, *Atmos. Meas. Tech.*, 2016, **9**, 5331–5346.

13 W. P. Arnott, H. Moosmüller, C. F. Rogers, T. Jin and R. Bruch, *Atmos. Environ.*, 1999, **33**, 2845–2852.

14 A. A. Kosterev, Y. A. Bakhirkin, R. F. Curl and F. K. Tittel, *Opt. Lett.*, 2002, **27**, 1902–1904.
15 M. B. Baker, *Atmos. Environ.*, 1967, **1976**(10), 241–248.
16 M. Kulmala, T. Vesala and P. Wagner, *J. Aerosol Sci.*, 1992, **23**, 133–136.
17 M. Kulmala and P. E. Wagner, *J. Aerosol Sci.*, 2001, **32**, 833–841.
18 R. Raspet, W. V. Slaton, W. P. Arnott and H. Moosmüller, *J. Atmospheric Ocean. Technol.*, 2003, **20**, 685–695.
19 D. M. Murphy, *Aerosol Sci. Technol.*, 2009, **43**, 356–363.
20 D. E. Day and W. C. Malm, *Atmos. Environ.*, 2001, **35**, 5169–5176.
21 T. Baynard, R. M. Garland, A. R. Ravishankara, M. A. Tolbert and E. R. Lovejoy, *Geophys. Res. Lett.*, 2006, **33**, L06813.
22 M.-J. Jeong, Z. Li, E. Andrews and S.-C. Tsay, *J. Geophys. Res.*, 2007, **112**, D10202.
23 P. Zieger, E. Kienast-Sjögren, M. Starace, J. von Bismarck, N. Bukowiecki, U. Baltensperger, F. G. Wienhold, T. Peter, T. Ruhtz, M. Collaud Coen, L. Vuilleumier, O. Maier, E. Emili, C. Popp and E. Weingartner, *Atmos. Chem. Phys.*, 2012, **12**, 7231–7249.
24 P. Zieger, R. Fierz-Schmidhauser, E. Weingartner and U. Baltensperger, *Atmos. Chem. Phys.*, 2013, **13**, 10609–10631.
25 J. Redemann, P. B. Russell and P. Hamill, *J. Geophys. Res.*, 2001, **106**, 27485–27495.
26 A. F. Khalizov, H. Xue, L. Wang, J. Zheng and R. Zhang, *J. Phys. Chem. A*, 2009, **113**, 1066–1074.
27 B. T. Brem, F. C. M. Gonzalez, S. R. Meyers, T. C. Bond and M. J. Rood, *Aerosol Sci. Technol.*, 2012, **46**, 178–190.
28 J. Michel Flores, R. Z. Bar-Or, N. Bluvshtein, A. Abo-Riziq, A. Kostinski, S. Borrmann, I. Koren, I. Koren and Y. Rudich, *Atmos. Chem. Phys.*, 2012, **12**, 5511–5521.
29 T. C. Bond, G. Habib and R. W. Bergstrom, *J. Geophys. Res.: Atmos.*, 2006, **111**, D20211.
30 R. E. Willoughby, M. I. Cotterell, H. Lin, A. J. Orr-Ewing and J. P. Reid, *J. Phys. Chem. A*, 2017, **121**, 5700–5710.
31 W. P. Arnott, H. Moosmüller, P. J. Sheridan, J. A. Ogren, R. Raspet, W. V. Slaton, J. L. Hand, S. M. Kreidenweis and J. L. Collett, *J. Geophys. Res.: Atmos.*, 2003, **108**(D1), 4034.
32 K. A. Lewis, W. P. Arnott, H. Moosmüller, R. K. Chakrabarty, C. M. Carrico, S. M. Kreidenweis, D. E. Day, W. C. Malm, A. Laskin, J. L. Jimenez, I. M. Ulbrich, J. A. Huffman, T. B. Onasch, A. Trimborn, L. Liu and M. I. Mishchenko, *Atmos. Chem. Phys.*, 2009, **9**, 8949–8966.
33 J. M. Langridge, M. S. Richardson, D. A. Lack, C. A. Brock and D. M. Murphy, *Aerosol Sci. Technol.*, 2013, **47**, 1163–1173.
34 D. A. Lack, P. K. Quinn, P. Massoli, T. S. Bates, D. Coffman, D. S. Covert, B. Sierau, S. Tucker, T. Baynard, E. Lovejoy, D. M. Murphy and A. R. Ravishankara, *Geophys. Res. Lett.*, 2009, **36**, L24805.
35 J. W. Cremer, K. M. Thaler, C. Haisch and R. Signorell, *Nat. Commun.*, 2016, **7**, 10941.
36 J. W. Cremer, P. A. Covert, E. A. Parmentier and R. Signorell, *J. Phys. Chem. Lett.*, 2017, **8**, 3398–3403.
37 R. Symes, R. M. Sayer and J. P. Reid, *Phys. Chem. Chem. Phys.*, 2004, **6**, 474–487.
38 M. I. Cotterell, B. J. Mason, T. C. Preston, A. J. Orr-Ewing and J. P. Reid, *Phys. Chem. Chem. Phys.*, 2015, **17**, 15843–15856.
39 A. Ashkin, *Phys. Rev. Lett.*, 1970, **24**, 156–159.
40 G. David, K. Esat, S. Hartweg, J. Cremer, E. Chasovskikh and R. Signorell, *J. Chem. Phys.*, 2015, **142**, 154506.
41 T. Li, S. Kheifets, D. Medellin and M. G. Raizen, *Science*, 2010, **328**, 1673–1675.
42 L. Rkiouak, M. J. Tang, J. C. J. Camp, J. McGregor, I. M. Watson, R. A. Cox, M. Kalberer, A. D. Ward and F. D. Pope, *Phys. Chem. Chem. Phys.*, 2014, **16**, 11426–11434.
43 Z. Gong, Y.-L. Pan, G. Videen and C. Wang, *J. Quant. Spectrosc. Radiat. Transfer*, 2018, **214**, 94–119.
44 Y. Q. Li, P. Davidovits, C. E. Kolb and D. R. Worsnop, *J. Phys. Chem. A*, 2001, **105**, 10627–10634.
45 J. F. Davies, R. E. H. Miles, A. E. Haddrell and J. P. Reid, *J. Geophys. Res.: Atmos.*, 2014, **119**, 10931–10940.
46 R. Hołyst, M. Litniewski, D. Jakubczyk, M. Zientara and M. Woźniak, *Soft Matter*, 2013, **9**, 7766–7774.
47 J. M. Langridge, M. S. Richardson, D. A. Lack and D. M. Murphy, *Geophys. Res. Lett.*, 2016, **43**, 6650–6656.
48 R. Marek and J. Straub, *Int. J. Heat Mass Transfer*, 2001, **44**, 39–53.
49 T. Raatikainen, R. H. Moore, T. L. Lathem and A. Nenes, *Atmos. Chem. Phys.*, 2012, **12**, 4227–4243.
50 P. M. Winkler, A. Vrtala, R. Rudolf, P. E. Wagner, I. Riipinen, T. Vesala, K. E. J. Lehtinen, Y. Viisanen and M. Kulmala, *J. Geophys. Res.: Atmos.*, 2006, **111**, D19202.
51 M. Zientara, D. Jakubczyk, K. Kolwas and M. Kolwas, *J. Phys. Chem. A*, 2008, **112**, 5152–5158.
52 J. D. Smith, C. D. Cappa, W. S. Drisdell, R. C. Cohen and R. J. Saykally, *J. Am. Chem. Soc.*, 2006, **128**, 12892–12898.
53 W. S. Drisdell, C. D. Cappa, J. D. Smith, R. J. Saykally and R. C. Cohen, *Atmos. Chem. Phys.*, 2008, **8**, 6699–6706.
54 R. E. H. Miles, J. P. Reid and I. Riipinen, *J. Phys. Chem. A*, 2012, **116**, 10810–10825.
55 C. E. Kolb, R. A. Cox, J. P. D. Abbatt, M. Ammann, E. J. Davis, D. J. Donaldson, B. C. Garrett, C. George, P. T. Griffiths, D. R. Hanson, M. Kulmala, G. McFiggans, U. Pöschl, I. Riipinen, M. J. Rossi, Y. Rudich, P. E. Wagner, P. M. Winkler, D. R. Worsnop and C. D. O'Dowd, *Atmos. Chem. Phys.*, 2010, **10**, 10561–10605.
56 Y.-Y. Su, A. Marsh, A. E. Haddrell, Z.-M. Li and J. P. Reid, *J. Geophys. Res.: Atmos.*, 2017, **122**, 12317–12334.
57 D. Jakubczyk, G. Derkachov, T. D. Duc, K. Kolwas and M. Kolwas, *J. Phys. Chem. A*, 2010, **114**, 3483–3488.
58 T. P. Wright, C. Song, S. Sears and M. D. Petters, *Aerosol Sci. Technol.*, 2016, **50**, 1385–1396.
59 J. P. D. Abbatt, A. K. Y. Lee and J. A. Thornton, *Chem. Soc. Rev.*, 2012, **41**, 6555–6581.
60 R. Rudolf, A. Vrtala, M. Kulmala, T. Vesala, Y. Viisanen and P. Wagner, *J. Aerosol Sci.*, 2001, **32**, 913–932.
61 J. Julin, P. M. Winkler, N. M. Donahue, P. E. Wagner and I. Riipinen, *Environ. Sci. Technol.*, 2014, **48**, 12083–12089.
62 V.-M. Kerminen, K. E. Lehtinen, T. Anttila and M. Kulmala, *Tellus B*, 2004, **56**, 135–146.
63 E. Ezhova, V.-M. Kerminen, K. E. J. Lehtinen and M. Kulmala, *Atmos. Chem. Phys.*, 2018, **18**, 2431–2442.
64 T. C. Preston, B. J. Mason, J. P. Reid, D. Luckhaus and R. Signorell, *J. Opt.*, 2014, **16**, 025702.

65 P. A. Covert, J. W. Cremer and R. Signorell, Proc. SPIE, Optical Trapping and Optical Micromanipulation XIV, 1034729, 2017.
66 H. A. Beck, R. Niessner and C. Haisch, *Anal. Bioanal. Chem.*, 2003, **375**, 1136–1143.
67 J. Rumble, *CRC Handbook of Chemistry and Physics*, CRC Press/Taylor & Francis Group, 99th edn, 2018.
68 T. D. C. Company, Tetraethylene glycol, Dow techreport 612-00005-0207X CRCG, 2007.
69 M. A. Stephens and W. S. Tamplin, *J. Chem. Eng. Data*, 1979, **24**, 81–82.
70 O. Iulian, A. Stefaniu, O. Ciocirlan and A. Fedeles, *UPB Bul. Stiint., Ser. B*, 2010, **72**, 37–44.
71 E. Sani and A. Dell'Oro, *Opt. Mater.*, 2014, **37**, 36–41.
72 D. R. Worsnop, M. S. Zahniser, C. E. Kolb, J. A. Gardner, L. R. Watson, J. M. Van Doren, J. T. Jayne and P. Davidovits, *J. Phys. Chem.*, 1989, **93**, 1159–1172.